Ultrafast carrier dynamics in microcrystalline silicon probed by time-resolved terahertz spectroscopy

L. Fekete, P. Kužel,* H. Němec, F. Kadlec, A. Dejneka, J. Stuchlík, and A. Fejfar
Institute of Physics, Academy of Sciences of the Czech Republic, Na Slovance 2, 182 21 Prague 8, Czech Republic
(Received 24 November 2008; revised manuscript received 27 January 2009; published 10 March 2009)

We present the results of optical-pump–terahertz probe experiments applied to a set of thin-film microcrystalline silicon samples, with structures varying from amorphous to fully microcrystalline. The samples were excited at wavelengths 800 and 400 nm and studied at temperatures down to 20 K. The character of nanoscopic electrical transport properties markedly change on a subpicosecond time scale. The initial transient photoconductivity of the samples is dominated by hot free carriers with a mobility of ~ 70 cm^2/Vs. These carriers are rapidly (within 0.6 ps) trapped into weakly localized hopping states. The hopping process dominates the terahertz spectra on the picosecond and subnanosecond time scales. The saturated high-frequency value of the hopping mobility is limited by the sample disorder in the amorphous sample and by electron-phonon interaction for microcrystalline samples.

DOI: 10.1103/PhysRevB.79.115306 PACS number(s): 72.20.−i, 78.47.jc, 73.50.−h

I. INTRODUCTION

Hydrogenated microcrystalline silicon (μc-Si:H) is a material with a wide range of potential applications not only in the solar cell industry, but also in the technology of active matrices of displays and other optoelectronic elements.[1] As it combines the advantages of crystalline silicon (c-Si), currently the most important material for electronic applications, with those of low-cost thin-film technology, it has become very attractive for large-area applications. The μc-Si:H has a complicated heterogeneous microstructure, which consists of a mixture of crystalline silicon grains, grain boundaries, voids, and amorphous silicon "tissue." Samples with different structure and therefore different electronic transport properties such as the lifetime and mobility of charge carriers can be prepared by tuning the deposition parameters. The lifetime and the mobility of the carriers on picosecond and nanosecond timescales are significantly influenced by the material structure (degree of crystallinity, grain arrangements, and sizes).

The methods classically used to investigate the photoconductivity of the samples, namely, transient photocurrent spectroscopy (TPC) and time-of-flight (TOF) spectroscopy,[2,3] are able to characterize the carrier transport over macroscopic distances (drift mobility) with a time resolution of about 10 ns or lower. However, the samples have to have ohmic contacts (TPC) or p-i-n structure (TOF). In contrast, the time-resolved terahertz spectroscopy[4,5] is a contact-free method able to follow the local ($\sim 1\times 10^{-7}$ m) in-plane motion of charges with a subpicosecond to nanosecond time resolution. With this time resolution it is possible to investigate the carrier transport within the nanostructural components and the different conductivity mechanisms may then appear simultaneously as different fingerprints in the time-resolved terahertz spectra (Drude-like conductivity, hopping, etc).[5,6] The investigation of the electronic hopping processes in disordered semiconductors in the terahertz range is of particular interest as this range may overlap with the frequency region where the hopping mechanism saturates and the related conductivity reaches its maximum. This regime is seldom observed in other experiments.

In this contribution we report on optical pump-terahertz probe (OPTP) experiments with a series of thin microcrystalline silicon (μc-Si:H) layers with different crystallinity. Preliminary results on these samples were presented in Ref. 6 with the following correspondence in the notation (a-C0 =Ca; C20=Cm1; C47=Cm2; C72=Cm3). Here we apply two different excitation wavelengths (400 and 800 nm) allowing us to probe the films to different depths. In addition, measurements at various temperatures (20, 100, 150, 300 K) provide a way to identify the origin of the observed localized states.

II. EXPERIMENTAL PART

A. Samples

We studied one fully amorphous (Ca) and three μc-Si samples (Cm1, Cm2, Cm3) prepared by plasma enhanced chemical vapor deposition (70 Pa; 250 °C; other deposition parameters are summarized in Table I). The hydrogen/silane dilution was adjusted to obtain samples with a different degree of crystallinity. The samples were deposited on $(1\bar{1}02)$-oriented $10\times 5\times 0.5$ mm^3 sapphire substrates and their thickness was measured by a surface profilometer Tencor AlphaStep.

The surface of the samples was investigated by ambient air Veeco atomic force microscope (Dimension 3100), yielding an average grain size and rms roughness of the samples

TABLE I. Deposition parameters and surface characteristics of samples; ρ_{rms} stands for the rms roughness of the surface.

Sample code	Thickness (nm)	RF power (W)	H_2/SiH_4	Grain size (nm)	ρ_{rms} (nm)
Ca	890 ± 50	9.5	12.8		5
Cm1	920 ± 50	9.5	23.8	720 ± 100	70
Cm2	770 ± 50	9.5	29.4	470 ± 50	22
Cm3	770 ± 50	9.7	47.6	280 ± 50	10

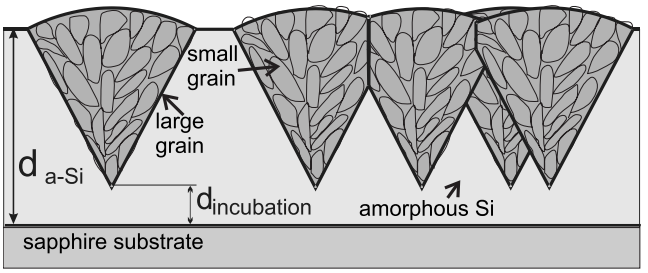

FIG. 1. Scheme of the crystalline grain growth in the amorphous matrix.

(Table I). The growth itself starts from isolated Si microcrystals from an amorphous incubation layer. The microcrystals are approximately spherically capped conical structures,[7,8] but once they collide during their growth, they create boundaries which are almost straight. The boundaries divide the sample area into natural neighboring areas available for the growth of each grain and this kind of growth can be modeled as a Voronoi tessellation.[9] As the grains are spherically capped, the increasing rms roughness is a measure of the increasing grain size (see Fig. 1).

B. Raman spectroscopy

Exact evaluation of the crystallinity in microcrystalline silicon is rather complicated[10,11] because of its complex structure. Consequently, several different methods for the decomposition of Raman spectra, leading to different values of crystallinity, can be found in the literature.[12–14] In our case, the crystallinity (Table II) was obtained from the decomposition of the Raman spectra into areas of amorphous and microcrystalline grain contributions,[14] taking into account the ratio of back-scattering cross sections of the phases.[15]

Several different excitation wavelengths were used: 442 nm (He-Cd laser), 514 nm (Ar+laser), 633 nm (He-Ne laser), and 785 nm (semiconductor diode laser). Since the light penetration depth decreases with increasing excitation wavelength, we could analyze the crystallinity from different depths of the samples.

Probing with 785 and 633 nm wavelength yields information about the average thin-film crystallinity (nominal penetration depths for the crystalline Si are 10 and 1.5 μm, respectively). In contrast, the penetration depths for excitation at 514 nm (0.25 μm) and 442 nm (40 nm) are smaller than the thickness of the samples and the crystallinity either near the front or near the back side of the thin film (illuminated then through the sapphire substrate) is obtained. Analogically, the entire film or only its surface are probed in the OPTP experiments with 800 and 400 nm excitation, respectively.

C. Spectroscopic ellipsometry

A quantitative evaluation of OPTP experiments requires the knowledge of initial concentration of photoexcited carriers, which is directly linked to the absorption coefficient of thin films. For this purpose, the optical properties of the fully amorphous and of the most crystalline samples (labeled Ca and Cm3, respectively) were studied using spectroscopic ellipsometry. Ellipsometric measurements were performed with a J. A. Woollam spectral ellipsometer working in the rotating analyzer mode at the incidence angle of 70°. A specially designed ultrahigh vacuum (UHV) cryostat system allowed the low-temperature measurements of ellipsometric angles Δ and Ψ at various wavelengths and at temperatures down to 20 K.

The spectral measurements were performed in the wavelength range from 350 to 1000 nm. It is well known that the absorption coefficients of Si at the wavelengths of interest, 400 and 800 nm, differ by about three orders of magnitude; furthermore, the layers exhibit a complex vertical microstructure on a scale comparable with the wavelength. For these reasons, the task to set up a layered model appropriate for the whole spectral range would be too complex. Instead, we have calculated effective optical constants separately in the intervals 375–425 and 775–825 nm, assuming a single homogeneous layer on an infinite substrate. The experimental data were analyzed with the software package WVASE32. The best agreement of our model with the experimental results was achieved for the values of surface roughness from 15 to 30 nm, which is consistent with the atomic force microscopy results. While this approximative approach does not guarantee a high precision of the values of the absorption coefficient, it is a reliable way of determining its relative changes with temperature, needed for the evaluation of OPTP experiments. The results are summarized in Table III. We stress that these results correctly reflect the temperature dependence of the absorption coefficient for our samples. In the cases when the absolute values at room temperature are

TABLE II. Raman crystallinity of the samples (in %); illumination from the front side (FS) and from the back side (BS).

Sample code	Excitation wavelength							
	442 nm		514 nm		633 nm		785 nm	
	FS	BS	FS	BS	FS	BS	FS	BS
Ca	0	0	0	0	0	0	0	0
Cm1	62	0	57	0	20	19	23	23
Cm2	75	3	73	67	52	53	58	58
Cm3	80	47	75	70	70	70	73	73

TABLE III. Temperature dependence of the absorption coefficient α [in cm^{-1}] of the samples Cm3 and Ca at 400 and 800 nm obtained by ellipsometry.

	Cm3		Ca	
Temperature	800 nm	400 nm	800 nm	400 nm
300 K	410	4.8×10^5	420	5.5×10^5
100 K	160	4.6×10^5	80	5.2×10^5
20 K	160	4.6×10^5	60	5.2×10^5

expected to play an important role, data from Ref. 16 are considered instead.

D. Time-resolved terahertz spectroscopy

The transient terahertz response was measured in a usual setup for OPTP experiments [Fig. 2(a)]. As a source of femtosecond laser pulses, we used a Ti:Sapphire laser amplifier with a 1 kHz repetition rate providing 60 fs pulses with the mean wavelength of 800 nm and the energy of 1 mJ per pulse. The pulse train was split into three branches. The first one (pump) was used for photoexcitation of the sample at 400 or 800 nm. The 400 nm wavelength was generated in an LBO crystal via second-harmonic generation. The second branch was used for generation of terahertz pulses via optical rectification in a 1 mm thick [011] ZnTe crystal. The terahertz pulses were subsequently used for probing the conductivity of the samples. The last (sampling) branch served for the phase-sensitive detection of the transmitted terahertz field using a gated electro-optic detection scheme in another [011] ZnTe crystal.[17] A lock-in detection synchronized to a mechanical chopper (166 Hz) placed either in the probe or in the pump branch was employed. Each of the three optical branches was equipped with a delay line to precisely adjust the time of the arrival of all pulses.[18] The whole terahertz setup was enclosed in a vacuum box to avoid the water vapor absorption. The holder of the samples had a clear aperture of 4 mm, which was larger than the diameter of the focused terahertz beam spot. To ensure a homogenous excitation of the samples the pump-beam diameter was stretched to 8 mm. Due to the substrate's birefringence the principal axes of the sapphire substrate were carefully aligned with the terahertz beam polarization using a pair of crossed wire-grid polarizers.

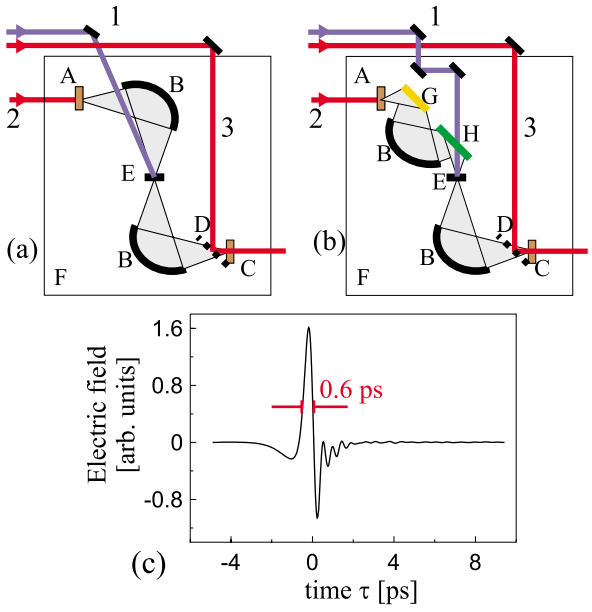

FIG. 2. (Color online) Experimental setup; configuration: (a) oblique arrangement, (b) collinear arrangement. 1: pump branch (400 nm, 800 nm), 2: terahertz probe branch, 3: sampling branch; A: ZnTe emitter, B: ellipsoidal mirrors, C: ZnTe sensor, D: pellicle beam splitter, E: sample, F: vacuum box, G: gold mirror, H: ITO-coated BK7 beam splitter; (c) wave form of a typical terahertz pulse.

In our experiments we used two different experimental geometries. A noncollinear setup [Fig. 2(a)] was used for the measurements of the slow dynamics (tens and hundreds of picoseconds). The oblique incidence of the excitation beam here caused a lower time resolution of the experiment ($\sim$1.5 ps). A better time resolution was achieved in the collinear experimental setup [Fig. 2(b)] where the whole probed area was excited at the same time. A key element of this setup is an indium tin oxide (ITO) coated optical glass (BK7) beam splitter. The ITO is highly conductive, thus acting as an efficient reflector for the terahertz pulses. At the same time, it is transparent for visible radiation. An antireflective coating was deposited on the rear side of the beam splitter to eliminate the losses of the excitation beam due to Fresnel reflections.

There are two modes of operation of the setup. In the first mode a time profile $E(\tau)$ of the electric field transmitted through the sample in equilibrium can be measured. In this case, the pump beam is blocked and the chopper is placed into the probe branch. The time variable τ describes the delay between the probing and the sampling pulses. In the second mode, the chopper is placed into the pump branch and the pump-induced changes in the terahertz electric field wave form $\Delta E(\tau, \tau_p)$, so-called transient wave form, is measured. The time variable τ_p stands for the delay between the pump and probe pulses.

For the 800 nm excitation wavelength the penetration depth in the microcrystalline silicon is about 25 μm (Table III), which largely exceeds the thickness of our samples. Thus, when using this wavelength, we obtain a transient terahertz response averaged over the whole depth of the samples. In contrast, the excitation wavelength of 400 nm, which has a penetration depth $\approx$40 nm, generates carriers only very close to the sample surface. The fact that sapphire is optically transparent allowed us to excite selectively either the front side or the back side of the samples, yielding information about the carrier dynamics either close to the free surface or close to the Si/sapphire interface, respectively. All experiments were carried out at the room temperature as well as at cryogenic temperatures (150, 100, 20 K).

III. RESULTS OF TIME-RESOLVED TERAHERTZ EXPERIMENTS

In our experiments as well as in photovoltaic applications free carriers are initially created by photoexcitation. These

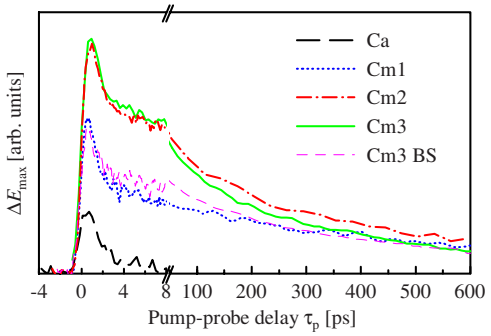

FIG. 3. (Color online) Pump-probe scans: maximum field amplitude of the transient terahertz signal $\Delta E_{\max}(\tau_p)$ versus pump-probe delay for samples excited at 400 nm at the room temperature.

carriers can be characterized by a delocalized wave function. Their interaction with terahertz radiation is typically very strong due to their high mobility. By contrast, if the carriers are captured in deep or shallow traps or if they are localized at grain boundaries by potential barriers, their motion can be described by a localized wave function and the carriers can be detected in terahertz experiments only if their resonant frequency lies near the terahertz range or if they remain mobile. These different types of behavior represent several contributions in the terahertz response with quite different spectral and temporal characteristics.

A. Pump-probe scans

The first insight into the kinetics of the photoexcited carriers is provided by pump-probe scans, in which the value of the maximum of the transient wave form $\Delta E_{\max}(\tau_p) \equiv \Delta E(\tau_0, \tau_p)$ (i.e., for a fixed $\tau = \tau_0$) is detected as a function of the pump-probe delay τ_p. It represents the time evolution of the mean terahertz response of the photoexcited sample, thus indicating the time scales on which the dynamical properties of the sample change. Pump-probe scans for all samples excited at 400 nm are displayed in Fig. 3. Two different time scales are observed; the first component is ultrafast (~1 ps) and it will be examined in Sec. III D, whereas the second (subnanosecond) one will be addressed in Sec. III C.

Generally speaking, there is a strong correlation between the signal amplitude and the crystallinity of the samples. In experiments with photoexcitation of the front side of the samples, the signal for the two most crystalline samples Cm3 and Cm2 (their front surface is fully microcrystalline) is higher than that for the least crystalline sample Cm1. The amorphous sample exhibits the weakest signal. Its averaged response consists only of the ultrafast subpicosecond component. The same, amorphouslike, behavior is also observed in Cm1 and Cm2 samples excited from the back side (not shown in the figure). The signal from the sample Cm3BS (i.e., Cm3 measured from the back side) is similar to that of Cm1 measured from the front side (Fig. 3), which means that the incubation layer of the sample Cm3 is smaller than the penetration depth of the 400 nm excitation wavelength.

The subnanosecond dynamics here is 2–3 times faster as compared to the pump-probe scans with 800 nm excitation (see Fig. 1 in Ref. 6). Since 400 nm excitation generates carriers in a thin layer (~40 nm), the capture of carriers in localized surface states can explain the acceleration of the dynamics. Note that the initial ultrafast part of the curves displayed here is broadened due to the limited time resolution of the noncollinear terahertz geometry used for these particular experiments.

B. Transient terahertz conductivity and permittivity

The main aim of this paper is to interpret the terahertz conductivity spectra which correspond to different parts of the dynamical evolution observed in Fig. 3. The information about the investigated dynamics is contained in the time-dependent transient conductivity $\Delta\sigma(\omega, \tau_p)$, where ω is the terahertz probing frequency and τ_p is the pump-probe delay. We rely on the well-known equivalence between the photoinduced conductivity $\Delta\sigma$ and relative permittivity $\Delta\epsilon$, i.e.,

$$\Delta\sigma = -i\omega\epsilon_0\Delta\epsilon. \tag{1}$$

Both quantities are complex

$$\Delta\sigma = \Delta\sigma_1 + i\Delta\sigma_2, \tag{2}$$

$$\Delta\epsilon = \Delta\epsilon_1 + i\Delta\epsilon_2, \tag{3}$$

describing the interaction of the terahertz radiation with localized and delocalized carriers on the same footing. We found that the most convenient representation to show the pertinent features in the spectra is to display the real parts of the two quantities, $\Delta\sigma_1$ and $\Delta\epsilon_1$, in the graphs. The real conductivity $\Delta\sigma_1$ represents losses (mainly of ohmic character) of the system and its extrapolation to zero frequency yields an estimation of the dc conductivity. The real part of the permittivity $\Delta\epsilon_1$ characterizes the dispersion of the system in terms of inductivelike (for negative contributions) or capacitivelike (for positive contributions) response.

The transient conductivity can be calculated from the photoinduced change $\Delta E(\omega, \tau_p)$ of the spectrum of broadband terahertz pulses transmitted through the sample. Note that it is in principle possible to investigate quantitatively processes faster than the terahertz pulse length.[4,18,19] In this case the frequency mixing of the terahertz pulse spectrum with that of the ultrafast response of the sample occurs.[20] Advanced methods of the data analysis must be then used to avoid artifacts in the conductivity spectra; namely, it is necessary to express the conductivity in two-dimensional (2D) frequency space (ω, ω_p), where ω_p is the angular frequency associated with the pump-probe delay time τ_p.[20] In the limit of small transient terahertz signal ($\Delta E \ll E_0$) the frequency mixing is expressed as in Ref. 21

$$\Delta E(\omega, \omega_p) = \Xi(\omega, \omega_p)\Delta\epsilon(\omega, \omega_p)E_0(\omega - \omega_p), \tag{4}$$

where E_0 is the terahertz field incident on the sample and Ξ is a transfer function, which was derived and discussed in detail in Ref. 21. In our case (thin film on the substrate) Ξ is proportional to $i\omega$.

If the signal decay is slower than the terahertz pulse length, so-called quasistatic approximation can be applied. This approximation assumes that the sample displays no evo-

lution of its state during the probing event [~1–2 ps, cf. Fig. 2(c)]. In other words, all the relevant dynamics are connected to small ω_p compared to the terahertz frequencies ($\omega_p \ll \omega$) and the frequency mixing in Eq. (4) can be neglected,

$$\Delta E(\omega,\omega_p) = \Xi(\omega,0)\Delta\epsilon(\omega,\omega_p)E_0(\omega), \tag{5}$$

or in the time (τ_p) domain

$$\Delta E(\omega,\tau_p) = \Xi(\omega,0)\Delta\epsilon(\omega,\tau_p)E_0(\omega). \tag{6}$$

C. Subnanosecond dynamics

1. Model

We first study the spectra related to the subnanosecond part using the above described quasistatic approximation. The transient conductivity $\Delta\sigma(\omega,\tau_p)$ is then extracted from Eqs. (6) and (1),

$$\Delta\sigma(\omega,\tau_p) = \frac{-i\omega\epsilon_0\Delta E(\omega,\tau_p)}{E_{\mathrm{ref}}(\omega)}\frac{T(\omega)}{\Xi(\omega,0)}, \tag{7}$$

where T is the equilibrium transmission spectrum of the sample and $E_{\mathrm{ref}}(\omega)$ is a reference wave form transmitted through the sample with the pump-beam blocked.

Generally, the dynamical response in the quasistatic approximation can be written in the factorized form

$$\Delta\sigma(\omega,\tau_p) = e\sum_i g_i(\omega)n_i(\tau_p), \tag{8}$$

where the sum is made over the individual contributions to the terahertz response; $g_i(\omega)$ describes the spectral response (i.e., frequency-dependent mobility) of the ith component and $n_i(\tau_p)$ corresponds to its carrier density decay.

In our previous paper[6] we analyzed the room-temperature data within a model comprising a Drude term and relaxation terms. The Drude model accounts for delocalized carriers,

$$g_D(\omega;\tau_D) = \frac{e}{m^*}\frac{1}{1/\tau_D - i\omega} = \mu_D\frac{1}{1-i\omega\tau_D}, \tag{9}$$

where τ_D is the momentum scattering time of the carriers; $\mu_D = \tau_D e/m^*$ is the dc limit of their microscopic mobility and m^* is their effective mass. Note that τ_D scales the amplitude of the conductivity and determines its spectrum. An important characteristic of this model is that the real part of the permittivity is negative ($\epsilon_1 < 0$) and that the dc conductivity is nonzero. In contrast, the response of localized carriers (case of hopping or localization within a well) is frequently described by an overdamped oscillator or Debye relaxator.[22] In the case of a Debye term with the relaxation frequency $1/\tau_R$ one gets

$$g_R(\omega;\tau_R) = \mu_R\frac{-i\omega}{1/\tau_R - i\omega}. \tag{10}$$

Carriers in this case feel a restoring force and, as a consequence, they do not contribute to the dc conductivity. The conductivity increases with frequency and in the high-frequency regime ($\omega\tau_R > 1$) it saturates; the coefficient μ_R then can be understood as a saturated high-frequency mobility.

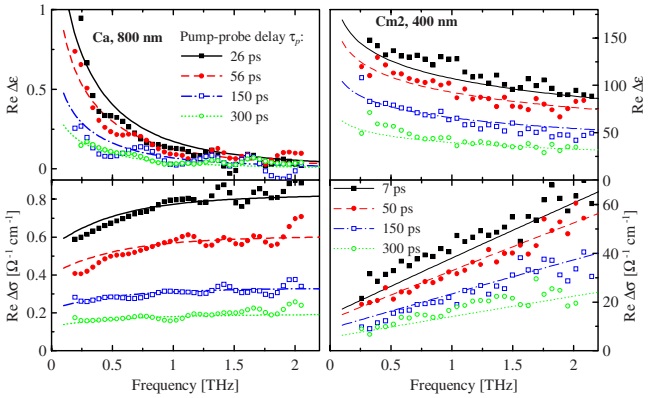

FIG. 4. (Color online) Examples of room-temperature transient spectra obtained for several pump-probe delays. Left panel: sample Ca, excitation at 800 nm, fitted by a single spectral response function (13) and the hyperbolic carrier population decay (15). Right panel: sample Cm2, excitation at 400 nm, fitted with Eq. (13) and the exponential carrier population decay (14). Symbols: experimental data, lines: fits.

In the case of the hopping conductivity more complex models should be used; their particular form reflects the underlying hopping mechanism. Here we used the model proposed by Dyre[23]

$$g_H(\omega) = i\omega\mu_H\left[1 - \frac{\ln(\tau_{\min}/\tau_{\max})}{\ln(1-i\omega\tau_{\min}) - \ln(1-i\omega\tau_{\max})}\right] \times \frac{\ln(\tau_{\max}/\tau_{\min})}{1/\tau_{\min} - 1/\tau_{\max}}, \tag{11}$$

where $1/\tau_{\max}$ and $1/\tau_{\min}$ are low and high cutoff frequencies, respectively, which roughly delimit the range of the conductivity dispersion. This model has qualitatively similar features to the Debye relaxator; however, it permits to describe the dispersion of the conductivity due to the hopping over several frequency decades as well as dc conduction.[23] Note that in real physical situations a drop of the conductivity due to the inertia of carriers must always occur above some threshold in the high-frequency regime. This is not taken into account either in Debye or in the above hopping model. However, our experimental data show that the dynamics we observe does not enter this regime.

2. Results and interpretation

The first series of experiments was carried out with 800 nm excitation; the initial density of photoexcited carriers, as estimated from the pump fluence impinging on the sample, was typically 1×10^{18} cm^{-3}. Examples of spectra obtained at different experimental conditions are shown in Figs. 4–6. In a previous paper the transient spectra obtained with 800 nm excitation at room temperature were interpreted in terms of a combination of Drude and relaxation terms,[6]

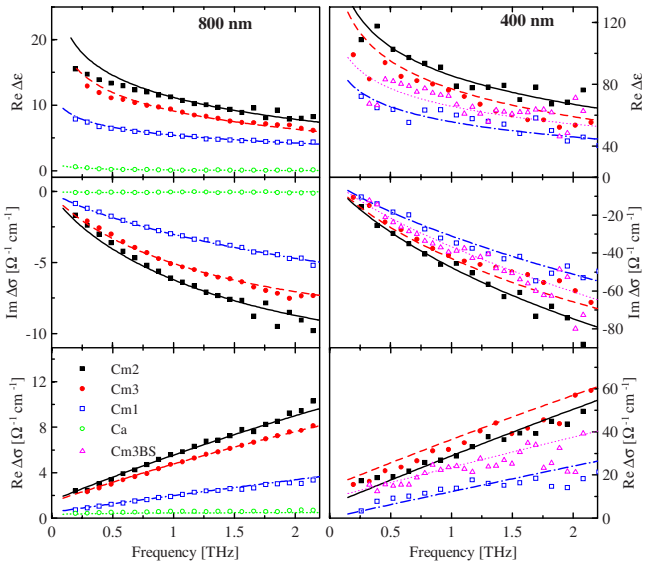

FIG. 5. (Color online) Real part of the transient permittivity (upper panel) and imaginary (middle panel) and real (lower panel) part of the transient conductivity for all samples; pump-probe delay: 50 ps; temperature: 300 K. Left part: pump at 800 nm, right part: pump at 400 nm. Symbols: experiment, curves: best fits based on Eq. (13).

$$\Delta\sigma(\omega,\tau_p)/e = g_D(\omega)n_D(\tau_p) + g_{R,\mathrm{slow}}(\omega)n_{R,\mathrm{slow}}(\tau_p) + g_{R,\mathrm{fast}}(\omega)n_{R,\mathrm{fast}}(\tau_p). \quad (12)$$

However, further investigation presented in the current paper has revealed that the expected temperature dependence of the pertinent model parameters within this interpretation would contradict the experimental data. These issues will be addressed in the discussion.

We think that the observed spectra can be understood within a hypothesis of a dominant hopping carrier transport, i.e., without a significant Drude-like contribution of the carriers. We assume that the activation of the hopping process occurs at frequencies much below the terahertz range ($1/\tau_{\max} \ll 1$ THz). Also our experimental data show that the conductivity drops with decreasing frequency in the subterahertz range and does not show any leveling off. In this regime Eq. (11) can be replaced by

$$g_H(\omega) = \mu_0 - i\omega\mu_H\tau_{\min}\ln[1 + i/(\omega\tau_{\min})], \quad (13)$$

where the static mobility μ_0 accounts for some conductivity process occurring below the accessible terahertz spectral range. This contribution is very small for all microcrystalline samples and our data do not allow discussing its origin. The subnanosecond charge transport in both microcrystalline and amorphous samples can be thus described by a single formula. The essential difference in the behavior of the samples consists in very different values of $\tau_{\min}$ and μ_H.

The same kind of fitting was performed for the data obtained with 400 nm excitation (see Figs. 4–6). Here the initial density of carriers is of about 5×10^{19} cm^{-3} and this explains the experimentally obtained higher values of the conductivity than for excitation at 800 nm. However, the number of carriers interacting with the terahertz wave is smaller than for the 800 nm excitation due to a much shorter absorption length. As a consequence the transient terahertz signal obtained with 400 nm pump is weaker and the corresponding conductivity data appear more noisy.

We found that the evolution of the carrier density n of microcrystalline samples can be well described by a single exponential decay with time constant θ_H,

$$n_H(\tau_p) = n_H(0)e^{-\tau_p/\theta_H}. \quad (14)$$

For the amorphous sample, the carrier density displays a hyperbolic decay (as previously observed also by optical pump-probe spectroscopy[24]),

$$n_H(\tau_p) = \frac{n_H(0)}{1 + \tau_p/\theta_H}. \quad (15)$$

An important quantity directly accessible from experimental data is the initial transient conductivity defined as

$$\sigma_H = e\mu_H n_H(0). \quad (16)$$

For each sample and each temperature transient spectra at several pump-probe delays were acquired (5–6 spectra for 800 nm excitation wavelength and 4–7 spectra for 400 nm excitation wavelength). The spectra for all measured pump-probe delays were fitted simultaneously in one global fit by Eq. (8) with a single spectral response function describing hopping process (13) and with a single function describing the population decay. Each curve presented in the figures is a result of this global fit for a particular pump-probe delay. For one sample and pump wavelength at a given temperature we thus have four fitting parameters (σ_0, σ_H, θ_H, $\tau_{\min}$) to describe 4–7 complex spectra. The quality of these fits can be checked in Fig. 4 for both excitation wavelengths. Note that we used the complex conductivity data in the fits; in this representation the low-frequency part of the spectrum has a smaller weight than in the permittivity plots. This is at the

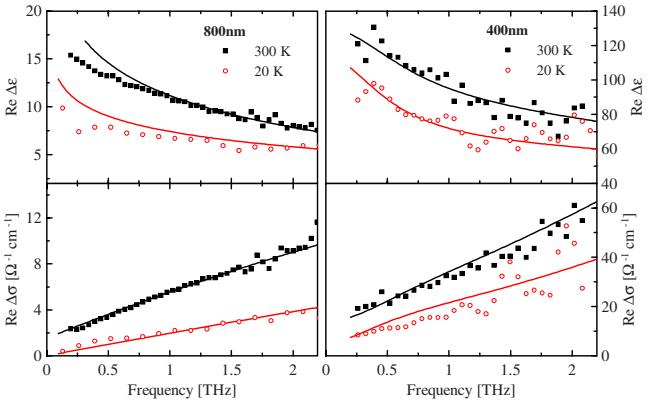

FIG. 6. (Color online) Real part of the transient complex permittivity (upper graphs) and conductivity (lower graphs) spectra of the sample Cm2 at pump-probe delay τ_p=50 ps. Left graphs were measured with 800 nm excitation, right graphs were obtained with 400 nm excitation. Points are measured data, curves represent the best fit by Eq. (13).

TABLE IV. Results of the temperature study (300→20 K) at 800 nm and 400 nm. * hyperbolic pump-probe decay; + only room-temperature measurements were performed.

	800 nm				400 nm			
Sample	θ_H (ps)	σ_H $[(\Omega\cdot\mathrm{cm})^{-1}]$	$\tau_{\min}$ (fs)	μ_H $[\mathrm{cm}^2/(\mathrm{Vs})]$	θ_H (ps)	σ_H $[(\Omega\cdot\mathrm{cm})^{-1}]$	$\tau_{\min}$ (fs)	μ_H $[\mathrm{cm}^2/(\mathrm{Vs})]$
Cm3	500→900	23→30	17→6.5	140→470	230→180	360→550	7.5→3	45→70
Cm2	400→1100	30→33	16.5→6.5	190→520	290→180	300→750	7.5→3	35→90
Cm1	650→800	24→15	7	150→230	+400	+480	+3	+60
Ca	+60*	+0.3	+160	+2				
Cm3BS+					+330	+540	+3	+65

origin of apparent small discrepancies found with some data at low frequencies in the real part of the permittivity (cf. samples Cm2 and Cm3 in Fig. 5).

The comparison of Re $\Delta\epsilon$ and Re $\Delta\sigma$ for 400 and 800 nm excitation wavelength measured at room temperature with pump-probe delay τ_p=50 ps is shown in Fig. 5. The two most crystalline samples exhibit clearly higher conductivity values in the terahertz range. A decrease in the conductivity is observed with decreasing crystallinity for both excitation wavelengths (samples Cm1 and Ca). The measurements Cm3BS (400 nm excitation from the back side) indicate a small decrease in the degree of crystallinity in a thin layer close to the substrate. For the amorphous sample no measurable response was observed for τ_p=50 ps at 400 nm (Fig. 3). The same is true for samples Cm2 and Cm1 excited from the back side: from this observation one may conclude that their structure close to the substrate should be similar to the amorphous one.

The low-temperature measurements were performed at 150, 100, and 20 K. Qualitatively, the samples exhibited the same response as at room temperature for both excitation wavelengths. This is illustrated in Fig. 6 for the Cm2 sample. The signal-to-noise ratio for the amorphous sample Ca excited by 800 nm wavelength and for microcrystalline samples Cm1 and Cm3BS excited at 400 nm was not high enough for a quantitative analysis; therefore only their room-temperature spectra were analyzed. A decrease in the transient conductivity and permittivity with decreasing temperature is systematically observed in the accessed spectral range for all other samples at both excitation wavelengths.

The compilation of the results of fits is shown in Table IV. The values for 400 nm excitation are determined with a larger experimental error; namely the displayed values of σ_H and $\tau_{\min}$, which are to some extent interconnected in the fit, should be understood as rough estimations for 400 nm pump. Nevertheless, some trends of the carrier behavior can be found out from a short inspection of the values shown. The lifetime of carriers seems to be shortened at the surface (probed with 400 nm excitation) in comparison with the average lifetime over the whole film (probed with 800 nm excitation). An important result of our study is the presence of a strong high-frequency dispersion (i.e., high values of high-frequency cutoff $1/\tau_{\min}$ in terms of the hopping model) in microcrystalline samples. This contribution strongly depends on crystallinity as observed in Table IV. The cutoff time $\tau_{\min}$ increases with the crystallinity and temperature for both excitation wavelengths. By contrast, the saturation of the hopping process is unambiguously observed in the amorphous sample (i.e., $1/\tau_{\min}$ lies in the terahertz spectral range).

The values found for Cm3BS are very similar to those obtained for Cm1 sample. The electrons close to the incubation layer of Cm3 should feel the same average environment as those at the front surface of Cm1 sample. The inner surface layers of Cm1 and Cm2 samples then should exhibit transport properties similar to those of fully amorphous sample.

On the one hand, the cooling leads to a decrease in terahertz and subterahertz response of all the samples, i.e., to the decrease in the accessible parts of Re $\Delta\sigma$ and Re $\Delta\epsilon$ (see Fig. 6). On the other hand, the fits of the most crystalline samples (Cm3 and Cm2) systematically indicate an increase in the saturated high-frequency conductivity σ_H at low temperatures (Table IV). This is essentially related to a systematic decrease in the value of $\tau_{\min}$ for these samples at low temperatures. Such a behavior may indicate a change in the character of the hopping process and will be further discussed.

Table IV summarizes also the electron hopping mobilities as found in our experiments. Note that these values are only rough estimations as for their evaluation the incident laser fluence and the absorption coefficient needs to be taken into account (absorption coefficient of Cm2 and Cm1 was assumed to have identical value to that of Cm3 for this evaluation). Nevertheless we deem that these values have at least semiquantitative validity.

D. Subpicosecond dynamics

1. Model

Determination of the transient conductivity for processes faster than the duration of the probing terahertz pulse, which clearly occur in our samples as observed in Fig. 3, requires the transformation of the data into the 2D frequency (ω,ω_p) space and the application of Eq. (4). The frequency mixing requires a proper deconvolution of the detector response. In Refs. 20 and 18 it was demonstrated that the transient conductivity can be directly calculated using the formula

$$\Delta\sigma(\omega,\omega_p) = -\mathrm{i}\omega\epsilon_0 \frac{T(\omega)\Delta E(\omega,\omega_p)E_0^D(\omega)\Psi(\omega-\omega_p)}{\Xi(\omega,\omega_p)E_{\mathrm{ref}}(\omega)E_0^D(\omega-\omega_p)\Psi(\omega)}, \tag{17}$$

where ΔE is the measured transient signal and E_{ref} is the reference signal obtained with the pump beam off; T is the complex equilibrium transmission function of the sample and Ξ is the transfer function from Eq. (4); E_0^D is the wave form incident on the sample as measured by replacing the sample by the sensor and Ψ is the sensor response function.

Models describing the carrier dynamics are then set up in the 2D frequency domain. The carrier concentration is assumed to exhibit an exponential decay in τ_p with a time constant θ'; i.e., we obtain in the frequency space for the jth process

$$n_j(\omega_p;\theta_j') = \frac{n_j(0)}{1/\theta_j' - \mathrm{i}\omega_p}. \tag{18}$$

The photoinduced complex Drude conductivity of the delocalized carriers is[19]

$$\Delta\sigma_D(\omega,\omega_p) = e g_D'(\omega;\tau_D',\theta_D')n_D(\omega_p;\theta_D'), \tag{19}$$

where the Drude mobility spectrum g_D' is similar to that defined by Eq. (9),

$$g_D'(\omega;\tau_D',\theta_D') = \frac{e}{m^*}\frac{1}{1/\tau_D' + 1/\theta_D' - i\omega}. \tag{20}$$

θ_D' is the carrier lifetime and $\tau_{D,\mathrm{eff}}' = (1/\tau_D' + 1/\theta_{\mathrm{D}}')^{-1}$ is an effective carrier momentum scattering time which adjoins the carrier trapping process as an additional damping mechanism to the usual collision term τ_D'; $n_D(0)$ is the initial carrier concentration. The conductivity shows a single pole at $\omega = \omega_p = 0$. The conductivity amplitude decreases with increasing frequencies; the speed of this decrease along ω and ω_p is a measure of $\tau_{D,\mathrm{eff}}'$ and θ_D', respectively.

The response of the Debye relaxator is a limiting case of an overdamped oscillator. Here we derive it simply from the response of a damped oscillator which was shown in Ref. 19. In terms of this reference, the Green's function of the ground state is $G_G = 0$ (no mobile carriers in the ground state); the relaxation time is $\tau_R' = \gamma_e/\omega_e^2$, where the eigenfrequency ω_e and damping γ_e in the excited state are much higher than the probing terahertz angular frequency ω. The response of the relaxator then reads

$$\Delta\sigma_R(\omega,\omega_p) = e g_R'(\omega;\tau_R',\theta_R')n_R(\omega_p;\theta_R'), \tag{21}$$

where θ_R' is the lifetime of the carriers. The mobility g_R' reads

$$g_R'(\omega;\tau_R',\theta_R') = \mu_R'\frac{1/\theta_R' - \mathrm{i}\omega}{1/\tau_R' + 1/\theta_R' - \mathrm{i}\omega} \tag{22}$$

and it is a analogous to the steady-state formula (10), where a renormalization owing to the additional damping mechanism θ_R' appears. Similarly as in the Drude model, the decay of the conductivity amplitude in the ω_p direction is connected to the carrier density lifetime θ_R'; note, however, that the conductivity is now an increasing function of the frequency ω.

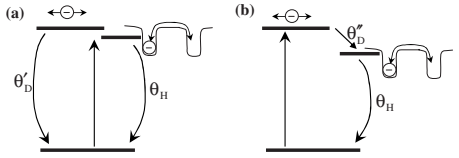

FIG. 7. Scheme of electron excitation from the valence band and their subsequent subpicosecond and subnanosecond decay within (a) parallel and (b) consecutive model.

Below we discuss two possible physical interpretations of the origin of the subpicosecond component. The first one (called parallel model) assumes that subnanosecond and subpicosecond conductivity mechanisms emerge instantaneously during the excitation event and that they are independent (i.e., the transfer of carrier population relative to the fast component into that of the slow component is negligible). The second interpretation is termed as a consecutive model and it assumes that the subnanosecond conductivity does not appear instantaneously, but it is a product of the decay of the subpicosecond component (i.e., it appears on the ultrafast scale progressively as the subpicosecond component vanishes). A scheme of the carrier decay within these two models is shown in Fig. 7.

2. Retrieval of the ultrafast dynamics

The measured data transformed to the frequency domain (ω,ω_p) are a mixture of the slow (subnanosecond) and the ultrafast (subpicosecond) contributions. The total transient conductivity is a sum of these components $[\Delta\sigma(\omega,\omega_p) = \Delta\sigma_{\text{sub-ns}}(\omega,\omega_p) + \Delta\sigma_{\text{sub-ps}}(\omega,\omega_p)]$. $\Delta\sigma_{\text{sub-ns}}$ has been analyzed independently and for the purpose of evaluation of $\Delta\sigma_{\text{sub-ps}}$ we can state

$$\Delta\sigma_{\text{sub-ns}} = e\sum_i g_i(\omega;\tau_i)n_i(\omega_p;\theta_i), \tag{23}$$

where g_i and n_i are identified with Drude and relaxation terms of Eq. (12). This is a purely formal mathematical assignment without physical insight which serves to reproduce the subnanosecond data by a model; note that Eq. (23) perfectly fits all the subnanosecond experimental data[6] and the Drude and relaxation mobilities g_D and g_R have their ultrafast counterparts in Eqs. (20) and (22), i.e., we can easily calculate g_D' and g_R' which will be needed later in Eq. (27).

The parallel mechanism of excitation, which assumes that subnanosecond and subpicosecond conductivity processes emerge instantaneously and that they are independent, can be described by the following conductivity:

$$\Delta\sigma(\omega,\omega_p) = e g_{\text{ps}}'(\omega;\tau_{\text{ps}},\theta_{\text{ps}})n_{\text{ps}}(\omega_p;\theta_{\text{ps}}) + \Delta\sigma_{\text{sub-ns}}(\omega,\omega_p), \tag{24}$$

where the fast component is termed by the index ps; n_{ps} describes the decay of the initial concentration of carriers participating in the fast process.

The consecutive mechanism of excitation assumes that the subnanosecond conductivity does not appear instantaneously, but it is a product of the decay of the subpicosecond

component. Assuming the photoexcitation event is instantaneous the conductivity owing to the fast component reads

$$\Delta\sigma_{\text{sub-ps}}(\omega,\tau_p) = en(0)g'_{\text{ps}}(\omega;\tau_{\text{ps}},\theta_{\text{ps}})Y(\tau_p)\exp(-\tau_p/\theta_{\text{ps}}), \tag{25}$$

where Y is the Heaviside function. The subnanosecond contribution appears on the ultrafast scale progressively as the subpicosecond component vanishes,

$$\Delta\sigma_{\text{sub-ns}}(\omega,\tau_p) = eY(\tau_p)n(0)\sum_i \frac{\theta_i}{\theta_i-\theta_{\text{ps}}} \times[g'_i(\omega;\tau_i,\theta_i)\exp(-\tau_p/\theta_i) - g'_i(\omega;\tau_i,\theta_{\text{ps}})\exp(-\tau_p/\theta_{\text{ps}})]. \tag{26}$$

Taking into account the fact that $g'_i(\omega;\tau_i,\theta_i)\approx g_i(\omega;\tau_i)$ for the subnanosecond components where $\theta_i \gg \tau_i$ we obtain for the total transient conductivity in the (ω,ω_p) space

$$\Delta\sigma(\omega,\omega_p) = eg'_{\text{ps}}(\omega;\tau_{\text{ps}},\theta_{\text{ps}})n(\omega_p;\theta_{\text{ps}}) + e\sum_i \frac{\theta_i}{\theta_i-\theta_{\text{ps}}}[g_i(\omega;\tau_i)n_i(\omega_p;\theta_i) - g'_i(\omega;\tau_{\text{ps}},\theta_{\text{ps}})n(\omega_p;\theta_{\text{ps}})]. \tag{27}$$

The ultrafast onset of the slowly decaying component is accounted for by the right-most term of this equation.

The parameters relevant for the subpicosecond dynamics are then allowed to vary in the fitting procedure while the parameters relative to the slow decay are held fixed. The subnanosecond and ns conductivity dominates around $\omega_p \approx 0$ while the subpicosecond conductivity extends much more in the ω_p direction. Here we are interested in the subpicosecond dynamics, therefore areas $|\omega_p/2\pi|<0.1$ THz were ignored in our fits.

3. Results and interpretation

The subpicosecond response was measured in the collinear experimental setup in Fig. 2(b) to achieve the ultimate time resolution. Our measurements and analysis followed the procedure described in Ref. 18. A set of transient wave forms $\Delta E(\tau,\tau_p)$ was measured for several pump-probe delays to obtain a dense 2D grid of data. Typically, we obtained a grid with the dimensions of 10×12 ps (100×120 points) for the 800 nm excitation and a grid with the dimensions of 6×5 ps (60×50 points) for the 400 nm excitation.

An example of the measured conductivity in the 2D frequency domain is shown in Fig. 8(a). The spectra consist of several segments, representing experimentally accessible areas.[20] The measured data transformed to the frequency domain (ω,ω_p) are a mixture of the slow (subnanosecond) and the ultrafast (subpicosecond) contributions and we retrieve the parameters of the ultrafast component following the procedure described in the previous paragraph.

Figures 8(b)–8(f) display the results of fits within the parallel model; the consecutive model provides a comparable quality of fits. Figure 8(b) shows the contribution of the subnanosecond dynamics in the 2D frequency domain. The subpicosecond contribution [Fig. 8(c)] exhibits a maximum for

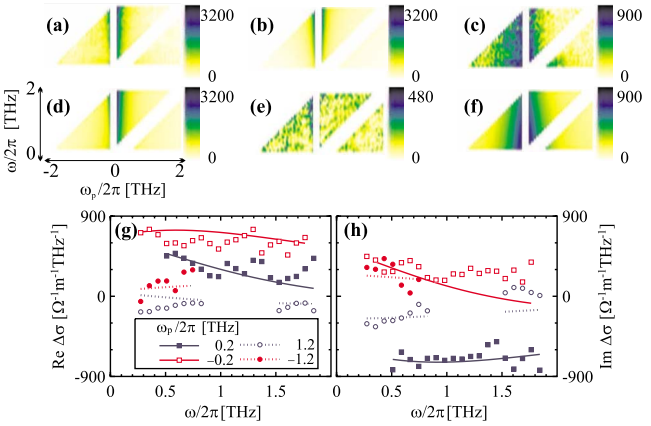

FIG. 8. (Color online) (a) Experimentally obtained amplitude of transient conductivity spectra $\Delta\sigma(\omega,\omega_p)$ [in Ω^{-1} m^{-1} THz^{-1}] of the sample Cm3 measured at room temperature and photoexcited at 800 nm; (b) experimental subnanosecond contribution; (c) retrieved subpicosecond contribution; (d) fit of the experimental data: sum of the subnanosecond contribution with fixed parameters and the subpicosecond contribution was fitted by the parallel Drude model; (e) residues of the fit; (f) resulting subpicosecond Drude contribution of the fitted complex conductivity; [(g) and (h)] examples of 1D slices of the complex transient conductivity; symbols: measured data corresponding to plot (c); lines: the best global fit of the data corresponding to plot (f).

$(\omega,\omega_p)=(0,0)$ and slowly decreases with frequency ω. This means that the ultrafast conductivity is dominated by a Drude response. Indeed, fitting the subpicosecond component by the Drude term is sufficient since it leads to a featureless spectrum of the residues [Fig. 8(e)]. The quality of the fit is best seen in one-dimensional cuts of the data in Figs. 8(g) and 8(h); note that by adjusting values of just a few parameters we get a close match of a large number of curves of which four are illustrated in the figure. The same model was successfully applied for fitting the spectra of all microcrystalline samples; however, the ultrafast dynamics of the amorphous sample shows broad poles at $\omega\neq0$ and could not be satisfactorily fitted by the simple Drude or relaxator model or their combination. We assume that a more complex hopping model would be needed to account for the observed features.

The results of the fits within the parallel approach are summarized in Table V. The momentum scattering time τ'_D and consequently the carrier mobility μ'_D were found to be crystallinity dependent and reached higher values for more crystalline samples. These values are close to a value observed in crystalline Si. The lifetime of free carriers θ'_D was found to be between 0.50–0.65 ps for all the samples; this lifetime can be considered identical within the experimental error. The amplitude of the slow component is significantly higher than that of the ultrafast one; this can be qualitatively observed in Fig. 3 of this paper for 400 nm pump and in Fig. 1 of Ref. 6 for 800 nm pump. Quantitatively, the fits show that within the parallel model only about 10%–20% of highly mobile (see Table V) photoexcited electrons contribute to the ultrafast component while the remaining 80%–90% of electrons participate in the slowly decaying hopping process.

TABLE V. Parameters of the ultrafast subpicosecond conductivity at 300 K for both 800 and 400 nm excitation; parallel model, fitting using a Drude term [Eq. (19)].

	800 nm			400 nm		
Sample	τ'_D (fs)	μ'_D (cm^2/Vs)	θ'_D (ps)	τ'_D (fs)	μ'_D (cm^2/Vs)	θ'_D (ps)
Cm3	90	610	0.55	55	370	0.55
Cm2	60	410	0.65	80	540	0.60
Cm1	55	370	0.55	70	470	0.55
Cm3BS				45	300	0.50

In the frame of the consecutive approach all the photoexcited electrons participate in the ultrafast process immediately after the excitation ($\tau_p=0$) and similarly as in the case of the parallel model they are found to exhibit the Drude behavior for all crystalline samples. The experimental data were successfully fitted within this model and their mobility was observed to be significantly lower as compared to that of the parallel approach; we found $\tau''_D \lesssim 10$ fs and $\mu''_D \lesssim 70$ cm^2/Vs for all microcrystalline samples. Within the consecutive model the decay times θ''_D display the same values as for the parallel model (θ'_D), $\theta''_D \approx 0.55-0.65$ ps.

IV. DISCUSSION

The structure of μc-Si:H consists of large grains surrounded by an amorphous tissue. The large grains with size of hundreds of nm are built of small grains with typical size of about 20 nm.[25] These two distinct length scales appear as different time scales in our time-resolved experiments. A characteristic time of the subpicosecond dynamics is $\theta'_D \approx 0.5$ ps (Table V). If we assume that the diffusion of the photogenerated electrons is the same as in c-Si ($D=36$ cm^2 s^{-1}), we find a characteristic length of $\sqrt{D\theta'_D}$ ~ 40 nm. The subpicosecond dynamics is then determined by intrinsic properties of small grains and/or by their boundaries, while the large grain boundaries may control only the subnanosecond dynamics.

Due to the inhomogeneity of μc-Si:H, one should carefully consider which parts of the sample can significantly contribute to the transient conductivity. Upon excitation at 800 nm the amorphous tissue absorbs considerably less than the c-Si and μc-Si:H (Ref. 16); however, the reverse can hold for excitation at 400 nm, where the beam is absorbed within a very thin layer which is almost crystalline in some samples for excitation at the front surface. This means that for both excitation wavelengths it is reasonable to assume that the majority of the pump photons is absorbed in crystalline parts of the films. Since the transient conductivity of the amorphous sample is smaller than that of the μc ones (Fig. 3), we neglect any possible contribution due to direct excitation of amorphous tissue when discussing the properties of μc samples.

The mobility of holes in c-Si is approximately four times lower than the mobility of electrons.[26] The contribution of electrons to the transient conductivity spectra is then expected to be dominant; however, there may be a small contribution of holes in the measured spectra as well. The subsequent discussion considers electrons only, but similar arguments can be reused to include also the hole dynamics.

A. Subpicosecond dynamics in μc samples

Within the parallel model, the ultrafast component of the conductivity spectra is accounted for by a single Drude term with a mobility comparable to that found in c-Si. From the amplitude of the subpicosecond conductivity and from the known excitation fluence we can estimate that within this hypothesis only a very low fraction of the absorbed photons would generate the mobile electrons (e.g., $\sim 20\%$ at 800 nm and $\sim 8\%$ at 400 nm for the Cm3 sample). Since we have ruled out that photons are absorbed in the amorphous tissue, the hypothesis of the parallel model would require to admit that a large majority of photogenerated electrons is captured into hopping states on a time scale shorter than the temporal resolution of the setup ($\lesssim 50$ fs) (while only a minority is captured with a quite longer time-constant of ~ 0.5 ps) or that localized hopping states are populated directly during the photoexcitation event.

In the consecutive model, we start from the assumption that all absorbed photons generate mobile electrons in the X valley of Si. The ultrafast drop in the conductivity then represents capturing the electrons in hopping states. The increase in occupation of the hopping states appears as a subpicosecond rise of the subnanosecond component. The conductivity of the nascent free electrons is well described by a Drude model with a low initial mobility $\mu''_D \lesssim 70$ cm^2 V^{-1} s^{-1}.

Both hypotheses lead to fits with a comparable quality. We believe that the consecutive model more properly reflects the photoinduced dynamics. A capture time shorter than 100 fs seems to interfere with the fact that μc-Si:H is a material with a high fraction of well crystalline component—most ultrafast materials are highly defective and rarely show such short lifetimes.[27] Moreover, the photogenerated carriers have very high excess energy which makes their efficient capture difficult.

Such discrepancies are not encountered in the consecutive model, and we show below that the speed of decay and the magnitude of the mobility are well explained by the fact that the carriers are initially hot. The initial electron temperature in c-Si upon photoexcitation at 800 nm is $T_{e,0} \approx 2000$ K, and the cooling occurs with a rate of a few hundreds of fs.[28,29] The mobility μ''_D then corresponds to electron temperature $T_e=1000$ K, which represents a reasonable estimate of an average electron temperature during the subpicosecond decay. Note that we did not observe any significant difference (either in amplitude or in time constants) in the ultrafast part of pump-probe scans within the broad investigated temperature range. The independence of these results on the lattice temperature corroborates the conclusion that hot carriers are responsible for the subpicosecond component. If the carriers were equilibrated with lattice then their mobility, decay time, and the ultrafast conductivity amplitude would be strongly temperature dependent.

Although we are far from equilibrium, we tentatively apply Einstein relation to estimate the diffusion coefficient: $D''=\mu''_D k_B T_e/e_0 \lesssim 5$ cm^2 s^{-1}. With these values, the diffusion length $\sqrt{D''\theta''_D}$ is less than ~ 17 nm, and it delimits the distance through which the electrons can travel prior to their relaxation to states with much lower mobility. The similarity of the small grain size and the diffusion length argues for an explanation that these states are located at the small-grain boundaries. Jepsen *et al.*[30] previously performed optical-pump–terahertz probe experiments without spectral resolution in μc-Si:H and observed a similar decay time of 0.7 ps, which they assigned to capture in trapping states. In our study, we have an additional spectral resolution which allows us to demonstrate that there is a slower transport process between these states which is responsible for the subnanosecond conductivity discussed in the next section. Ultrafast dynamics in microcrystalline silicon was studied also by optical transient absorption technique;[31] in this work the authors observed a fast 240-fs component which was independent of the crystallinity degree of the investigated samples. This component has been attributed to the intraband relaxation of hot carriers within crystallites. This component, even if twice faster, should have the same origin as that observed in our experiments.

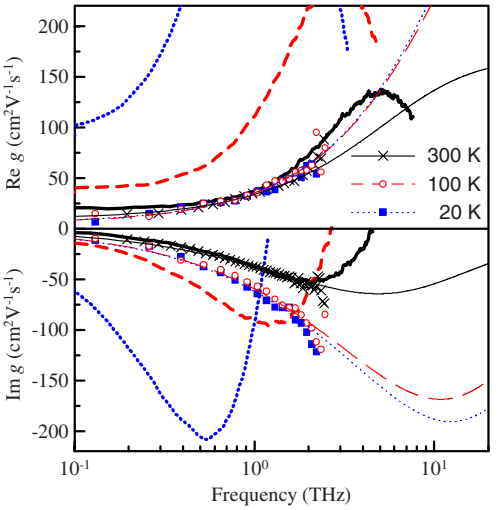

FIG. 9. (Color online) Mobility spectra of the subnanosecond contribution (pump-probe delay $\tau_p=50$ ps) of Cm2 sample for several temperatures; pump wavelength: 800 nm. Symbols: experimental data, thick lines: results of the Monte Carlo simulation described in the text (grain size 20 nm, grain-boundary permeability 1%), thin lines: extrapolation of the fit of the data by hopping model (13).

B. Subnanosecond dynamics in μc:H samples

It has been demonstrated in the previous section that the character of the carrier transport changes at about 0.6 ps after photoexcitation event. The observed slow component decays on a subnanosecond time scale in agreement with previously published data obtained by optical transient grating technique.[32] The aim of this paragraph is to attribute the observed signal to the underlying transport processes.

1. Absence of Drude contribution

In our previous paper[6] we showed that the room-temperature spectra can be well fitted by a sum of three terms: a Drude term, a relaxation in the 3–7 terahertz range (fast relaxation) and a relaxation in the subterahertz range (slow relaxation). We found that all the temperature dependent data can be fitted by this model; the amplitudes of these terms (as it can be expected from the experimental data shown in Fig. 6) decrease with decreasing temperature. The aim of this paragraph is to refute this hypothesis with physical arguments.

It was shown that no fast relaxation contribution is observed in the amorphous sample and that its characteristic decay time in microcrystalline samples is similar to that of the Drude term.[6] This suggested us a hypothesis that the process could be connected to the localization of free carriers within nanoscopic crystalline grains. Similar picture has been recently proposed to explain photoexcited carrier dynamics in Si nanocrystals embedded in SiO_2 matrix.[33] Within such a model the conduction-band carriers would exhibit two fingerprints in the spectra: a localized contribution occurring at 3–7 terahertz and a delocalized (Drude-like) one. We made an attempt to model the transport of electrons inter and intragrains using a Monte Carlo method. In brief, we simulated a thermal motion of free electrons in spherical potential wells representing crystalline grains. Inside the spheres the electron momentum randomly changes with a mean time τ_s between the scattering events. This scattering time, which characterizes in fact the microscopic intragrain mobility, is temperature dependent similarly as that in crystalline silicon;[26,34] in our simulations we used the room-temperature value of the crystalline silicon mobility and its temperature dependence which was reported for moderately doped silicon.[26] Upon hitting the grain boundary an electron can enter into the neighboring grain with some probability p (describing the permeability of the boundaries for conduction electrons). The spectral response of electrons was then calculated using Kubo formula;[35] more details are provided in Ref. 36.

We found that our room-temperature data are quantitatively well described by this model provided the involved grains have a 20–30 nm size and provided the permeability of the grain boundaries is $p \approx 1\%$ (i.e., one particle out of 100 will pass through the boundary without feeling the localization). The results are shown in Fig. 9. When larger grains and/or higher permeability of the grain boundaries are introduced into the simulation the resulting dc mobility reaches significantly higher values and cannot reproduce the experimental data. The found extent of the carrier localization (20–30 nm) then implies the leading role of the so-called "small grains"[37] in this process. On the other hand, these small grains cause only a small perturbation in the drift mobility of free electrons.[25] This is in a contrast with the requirement of our simulation of the very low permeability of the grain boundaries for conduction electrons.

Even more severe discrepancy is found if we compare the results of the low-temperature experiments with the results of the simulation. Besides the temperature dependent intra-

grain mobility mentioned above the response also significantly changes due to the variation in the thermal velocity of carriers $v=\sqrt{3k_BT_e/m^*}$ (the carriers were assumed to be thermalized with the lattice for subnanosecond process). The data in Fig. 9 clearly indicate that both the dc mobility and the localization effects (apparent namely in Im g) yielded by the simulation highly overestimate the mobility deduced from the experiment. We deem that these severe discrepancies invalidate the use of the Drude model for the interpretation of the subnanosecond dynamics in our sample, and we propose a hopping model as an alternative.

2. Hopping dynamics

The initially hot free carriers relax within 0.6 ps to the hopping states of microcrystalline silicon. There are practically no delocalized carriers after this time.

Let us stress here that μ_H and $\tau_{\min}$ are to some extent correlated in the fits of microcrystalline samples as the saturation plateau is not directly observed within the accessible terahertz spectral range. Therefore we should consider the values found in the fits as an order of magnitude estimates of the true values. Nevertheless, the saturated high-frequency mobilities μ_H are an order of magnitude lower than the low-frequency Drude mobilities in the crystalline silicon ($\approx$1400 cm^2/Vs at room temperature for a good quality crystal). This means that the carriers in microcrystalline samples exhibit a strong response in the high-frequency regime.

An estimate for Cm2 and Cm3 of $\tau_{\min}\sim 16$ fs at room temperature corresponds to a cutoff frequency of 10 terahertz and $\tau_{\min}\sim 7$ fs obtained at low temperatures corresponds to a cutoff frequency of 22 terahertz. Figure 9 displays an example of the mobility spectra obtained for Cm2 sample. The real part of the mobility exhibits quantitatively the same behavior in the terahertz spectral range between 20 and 300 K. This indicates that the character of the carrier transport does not change with temperature, and it is compatible with the hypothesis of largely dominating hopping process provided our spectral range is close to the high-frequency cut $1/\tau_{\min}$. The different slopes of the negative imaginary conductivity for the room and low temperatures are connected to the shift of the conductivity minimum, i.e., to the shift of $1/\tau_{\min}$ with temperature this trend can be clearly observed in Table IV in all microcrystalline samples. The fact that the saturation shifts to higher frequencies at low temperatures is connected in turn to the different values of the saturated real part of the mobility mobility. This suggests that the hopping of carriers is hindered by some scattering mechanisms which limit the upper hopping frequency and the maximum hopping conductivity; the experimental results suggest that these mechanisms may become less efficient at low temperatures in microcrystalline samples.

In the amorphous sample Ca the saturation frequency $1/\tau_{\min}$ falls into the terahertz range as observed in Figs. 4 and 5 and it is about an order of magnitude lower than that in the microcrystalline samples. In addition the saturated hopping mobility is nearly two orders of magnitude lower than that for the microcrystalline samples. We believe that the hopping is strongly limited by the disorder in the amorphous phase.

The optical phonon frequency in Si is 16 THz. In this respect the saturation process of the hopping in samples with a high crystallinity could be related to the interaction of carriers with the optical phonon. At 20 K, when the phonon states are not populated, the saturation is systematically observed at higher frequency. This is correlated with the increase in μ_H at low temperatures which indicates deactivation of the electron-phonon scattering mechanism.

Note that the values of the mobility obtained for experiments with 400 nm are systematically about $3-5\times$ lower than those obtained for 800 nm. This suggests that the carrier-carrier scattering mechanisms starts to strongly influence the transport: the terahertz mobilities obtained for significantly higher carrier concentrations are reduced by the carrier-carrier scattering.

The Cm3BS sample (back side, 400 nm) exhibits an intermediate behavior between the most crystalline samples (Cm2 and Cm3) and the sample with intermediate crystallinity (Cm1). It is interesting to note a large value of $1/\tau_{\min}$ found for Cm1, i.e., the sample close to the amorphous/microcrystalline transition, which is reminiscent of the maximum of ambipolar diffusion length typically observed at this transition (see, e.g., Ref. 38). This finding can be rationalized as the effect of the growth on the internal structure of the grains: the contribution of the crystallites increases with the increasing crystallinity until the grains collide and mutually hinder the further evolution of the ordered crystalline regions.

V. CONCLUSION

We have investigated, using time-resolved terahertz spectroscopy, ultrafast photoinduced conductivity of three microcrystalline samples with different degrees of crystallinity (23, 58, 73 %) and compared it to the conductivity of a fully amorphous sample. The experiments were carried out at temperatures between 300 and 20 K.

Two distinct dynamical regimes were found. We have shown that in the subpicosecond regime, the hot conduction carriers exhibit a bandlike transport described by a Drude contribution. The ultrafast decay is a result of carrier capture in shallow states at small-grain boundaries. After this initial phase—on the picosecond and nanosecond time scales—hopping of carriers among the shallow states becomes the dominating transport mechanism. Our analysis has shown that the Drude conductivity complemented with the charge localization in microcrystalline grains is not able to describe the ensemble of time-resolved spectra: in particular, these hypotheses are in contradiction with the measured temperature dependence.

In the relevant literature the terms and values of drift and microscopic (band) mobility are distinguished and frequently discussed.[39] The former one characterizes a macroscopic long-range transport between electrodes, and it accounts for carrier trapping and thermal activation in localized states across the sample while the latter one (investigated in this paper) is understood as a carrier local property. Following

our experiments the low-frequency mobility of the observed hopping process is of the order of 20 cm^2/Vs. This value is in agreement with the estimations of the microscopic mobility obtained by means of transient photocurrent or time-of-flight spectroscopies in μc-Si:H samples. The results of this work then indicate that the microscopic mobility is of hopping nature in microcrystalline silicon.

ACKNOWLEDGMENTS

We thank J. Kočka and M. Ledinský for valuable discussions. This research was supported by the Ministry of Education (Project No. LC06040) and by the Academy of Sciences of the Czech Republic (Project Nos. A100100902, AVOZ10100520, and AVOZ10100521).

*kuzelp@fzu.cz

[1] A. Shah, P. Torres, R. Tscharner, N. Wyrsch, and H. Keppner, Science **285**, 692 (1999).
[2] S. Reynolds, Mater. Res. Soc. Symp. Proc. **910**, 3 (2007).
[3] M. Brinza, J. Willekens, M. L. Benkhedir, E. V. Emelianova, and G. J. Adriaenssens, J. Mater. Sci.: Mater. Electron. **16**, 703 (2005).
[4] C. A. Schmuttenmaer, Chem. Rev. **104**, 1759 (2004).
[5] F. A. Hegmann, O. Ostroverkhova, and D. G. Cooke, *Photophysics of Molecular Materials* (Wiley-VCH, New York, 2006), Chap. 7, pp. 367–428.
[6] L. Fekete, H. Němec, F. Kadlec, P. Kužel, J. Stuchlík, A. Fejfar, and J. Kočka, J. Non-Cryst. Solids **352**, 2846 (2006).
[7] H. Fujiwara, M. Kondo, and A. Matsuda, Phys. Rev. B **63**, 115306 (2001).
[8] S. Koynov, S. Grebner, P. Radojkovic, E. Hartmann, R. Schwarz, L. Vasilev, R. Krankenhagen, I. Sieber, W. Henrion, and M. Schmidt, J. Non-Cryst. Solids **198-200**, 1012 (1996).
[9] A. Fejfar, T. Mates, O. Čertík, B. Rezek, J. Stuchlík, I. Pelant, and J. Kočka, J. Non-Cryst. Solids **338-340**, 303 (2004).
[10] M. Ledinský, L. Fekete, J. Stuchlík, T. Mates, A. Fejfar, and J. Kočka, J. Non-Cryst. Solids **352**, 1209 (2006).
[11] M. Ledinský, A. Vetushka, J. Stuchlík, T. Mates, A. Fejfar, J. Kočka, and J. Štěpánek, J. Non-Cryst. Solids **354**, 2253 (2008).
[12] M. Kondo, Y. Toyoshima, A. Matsuda, and K. Ikuta, J. Appl. Phys. **80**, 6061 (1996).
[13] D. Han, K. Wang, J. M. Owens, L. Gedvilas, B. Nelson, H. Habuchi, and M. Tanaka, J. Appl. Phys. **93**, 3776 (2003).
[14] C. Smit, R. A. C. M. M. van Swaaij, H. Donker, A. M. H. N. Petit, W. M. M. Kessels, and M. C. M. van de Sanden, J. Appl. Phys. **94**, 3582 (2003).
[15] R. Tsu, J. Gonzalez-Hernandez, S. S. Chao, S. C. Lee, and K. Tanaka, Appl. Phys. Lett. **40**, 534 (1982).
[16] A. Poruba, J. Springer, L. Mullerova, A. Beitlerova, M. Vaněček, N. Wyrsch, and A. Shah, J. Non-Cryst. Solids **338-340**, 222 (2004).
[17] A. Nahata, A. S. Weling, and T. F. Heinz, Appl. Phys. Lett. **69**, 2321 (1996).
[18] H. Němec, F. Kadlec, C. Kadlec, P. Kužel, and P. Jungwirth, J. Chem. Phys. **122**, 104504 (2005).
[19] H. Němec, F. Kadlec, S. Surendran, P. Kužel, and P. Jungwirth, J. Chem. Phys. **122**, 104503 (2005).
[20] H. Němec, F. Kadlec, and P. Kužel, J. Chem. Phys. **117**, 8454 (2002).
[21] P. Kužel, F. Kadlec, and H. Němec, J. Chem. Phys. **127**, 024506 (2007).
[22] S. R. Elliott, Adv. Phys. **36**, 135 (1987).
[23] J. C. Dyre, J. Appl. Phys. **64**, 2456 (1988).
[24] J. Kudrna, P. Malý, F. Trojánek, J. Štěpánek, T. Lechner, I. Pelant, J. Meier, and U. Kroll, Mater. Sci. Eng., B **69-70**, 238 (2000).
[25] J. Kočka, H. Stuchlíková, J. Stuchlík, B. Rezek, T. Mates, V. Švrček, P. Fojtik, I. Pelant, and A. Fejfar, J. Non-Cryst. Solids **299-302**, 355 (2002).
[26] F. J. Morin and J. P. Maita, Phys. Rev. **96**, 28 (1954).
[27] J.-L. Coutaz, Acta Phys. Pol. A **102**, 495 (2002).
[28] A. J. Sabbah and D. M. Riffe, Phys. Rev. B **66**, 165217 (2002).
[29] J. R. Goldman and J. A. Prybyla, Phys. Rev. Lett. **72**, 1364 (1994).
[30] P. Uhd Jepsen, W. Schairer, I. H. Libon, U. Lemmer, N. E. Hecker, M. Birkholz, K. Lips, and M. Schall, Appl. Phys. Lett. **79**, 1291 (2001).
[31] K. E. Myers, Q. Wang, and S. L. Dexheimer, Phys. Rev. B **64**, 161309(R) (2001).
[32] J. Kudrna, F. Trojánek, P. Malý, and I. Pelant, Appl. Phys. Lett. **79**, 626 (2001).
[33] D. G. Cooke, A. N. MacDonald, A. Hryciw, J. Wang, Q. Li, A. Meldrum, and F. A. Hegmann, Phys. Rev. B **73**, 193311 (2006).
[34] P. Norton, T. Braggins, and H. Levinstein, Phys. Rev. B **8**, 5632 (1973).
[35] R. Kubo, Rep. Prog. Phys. **29**, 255 (1966).
[36] H. Němec, P. Kužel, and V. Sundström, Phys. Rev. B (to be published).
[37] J. Kočka, H. Stuchlíková, J. Stuchlík, B. Rezek, V. Švrček, P. Fojtík, I. Pelant, and A. Fejfar, in *Polycrystalline Semiconductors: VI. Bulk Materials, Thin Films, and Devices*, edited by O. Bonnaud, T. Mohammed-Brahim, H. P. Strunk, and J. H. Werner, Solid State Phenomena Vols. 80–81 (Scitech, Uettikon am See, Switzerland, 2001), pp. 213–224.
[38] J. Kočka, T. Mates, H. Stuchlíková, J. Stuchlík, and A. Fejfar, Thin Solid Films **501**, 107 (2006).
[39] E. A. Schiff, J. Phys.: Condens. Matter **16**, S5265 (2004).